Quasi-analytical model for scattering infrared near-field microscopy on layered systems

Benedikt Hauer, Andreas P. Engelhardt, and Thomas Taubner[*]

Institute of Physics (IA), JARA – Fundamentals of Future Information Technologies RWTH Aachen University, 52056 Aachen, Germany

[*]*taubner@physik.rwth-aachen.de*

Abstract: We present a quantitative quasi-analytical model to predict and analyze signals on layered samples measured by infrared scattering-type scanning near-field optical microscopy. Our model predictions are compared to experimental data and to fully retarded calculations based on a point dipole approximation of the tip. The model is used to study the influence of the tip vibration amplitude and of the tip radius on the near-field contrasts of samples with particularly small variations in the layer thickness. Additionally the influence of a dielectric capping layer on the tip–substrate coupling is analyzed. When inversely applied, our calculation opens the possibility to extract the local layer thickness of thin films or the dielectric functions that allow one to draw conclusions on the material composition, conductivity or crystal structure on the nanoscale.

References and links

1. G. Friedbacher and H. Bubert, eds., *Surface and Thin Film Analysis*, 2nd ed. (Wiley-VCH, Weinheim, 2011).
2. Y. Inouye and S. Kawata, "Near-field scanning optical microscopy with a metallic probe tip," Opt. Lett. **19**, 159–161 (1994).
3. F. Zenhausern, Y. Martin, and H. K. Wickramasinghe, "Scanning interferometric apertureless microscopy: Optical imaging at 10 angstrom resolution," Science **269**, 1083–1085 (1995).
4. H. Kuzmany, *Solid State Spectroscopy*, 2nd ed. (Springer, Berlin, Heidelberg, 2009), Chap. 10.
5. F. Keilmann and R. Hillenbrand, "Near-field nanoscopy by elastic light scattering from a tip," in A. Zayats and D. Richards, eds., *Nano-optics and near-field optical microscopy* (Artech House, Boston, London, 2009), Chap. 11, pp. 235–265.
6. M. Born and E. Wolf, *Principles of Optics*, 7th ed. (Cambridge University Press, 1999), Section 8.6.
7. T. Taubner, R. Hillenbrand, and F. Keilmann, "Performance of visible and mid-infrared scattering-type near-field optical microscopes," J. Microscopy **210**, 311–314 (2003).
8. A. J. Huber, A. Ziegler, T. Köck, and R. Hillenband, "Infrared nanoscopy of strained semiconductors," Nature Nanotech. **4**, 153–157 (2009).
9. A. Huber, N. Ocelić, T. Taubner, and R. Hillenbrand, "Nanoscale resolved infrared probing of crystal structure and of plasmon–phonon coupling," Nano Lett. **6**, 774–778 (2006).
10. N. Ocelić and R. Hillenband, "Subwavelength-scale tailoring of surface phonon polaritons by focused ion-beam implantation," Nature Mat. **3**, 606–609 (2004).
11. J. M. Stiegler, A. J. Huber, S. L. Diedenhofen, J. G. Rivas, R. E. Algra, E. P. A. M. Bakkers, and R. Hillenband, "Nanoscale free-carrier profiling of individual semiconductor nanowires by infrared near-field nanoscopy," Nano Lett. **10**, 1387–1392 (2010).
12. M. B. Raschke and C. Lienau, "Apertureless near-field optical microscopy: Tip–sample coupling in elastic light scattering," Appl. Phys. Lett. **83**, 5089–5091 (2003).

13. T. Taubner, F. Keilmann, and R. Hillenband, "Nanoscale-resolved subsurface imaging by scattering-type near-field optical microscopy," Opt. Express **13**, 8893–8899 (2005).

14. J. Aizpurua, T. Taubner, F. J. García de Abajo, M. Brehm, and R. Hillenband, "Substrate-enhanced infrared near-field spectroscopy," Opt. Express **16**, 1529–1545 (2008).

15. A. Cvitković, N. Ocelić, J. Aizpurua, R. Guckenberger, and R. Hillenbrand, "Infrared imaging of single nanoparticles via strong field enhancement in a scanning nanogap," Phys. Rev. Lett. **97**, 060801 (2006).

16. A. Cvitković, N. Ocelić, and R. Hillenbrand, "Material-specific infrared recognition of single sub 10 nm particles by substrate-enhanced scattering-type near-field microscopy," Opt. Express **16**, 7453–7459 (2008).

17. J. M. Stiegler, Y. Abate, A. Cvitković, Y. E. Romanyuk, A. J. Huber, S. R. Leone, and R. Hillenband, "Nanoscale infrared absorption spectroscopy of individual nanoparticles enabled by scattering-type near-field microscopy," ACS Nano **5**, 6494–6499 (2011).

18. M. Brehm, T. Taubner, R. Hillenband, and F. Keilmann, "Infrared spectroscopic mapping of single nanoparticles and viruses at nanoscale resolution," Nano Lett. **6**, 1307–1310 (2006).

19. T. Taubner, D. Korobkin, Y. Urzhumov, G. Shvets, and R. Hillenband, "Near-field microscopy through a SiC superlens," Science **313**, 1595–1595 (2006).

20. Z. Fei, G. O. Andreev, W. Bao, L. M. Zhang, A. S. McLeod, C. Wang, M. K. Stewart, Z. Zhao, G. Dominguez, M. Thiemens, M. M. Fogler, M. J. Tauber, A. H. Castro-Neto, C. N. Lau, F. Keilmann, and D. N. Basov, "Infrared nanoscopy of Dirac plasmons at the graphene–SiO_2 interface," Nano Lett. **11**, 4701–4705 (2011).

21. L. M. Zhang, G. O. Andreev, Z. Fei, A. S. McLeod, G. Dominguez, M. Thiemens, A. H. Castro-Neto, D. N. Basov, and M. M. Fogler, "Near-field spectroscopy of silicon dioxide thin films," Phys. Rev. B **85**, 075419 (2012).

22. B. B. Akhremitchev, Y. Sun, L. Stebounova, and G. C. Walker, "Monolayer-sensitive infrared imaging of DNA stripes using apertureless near-field optical microscopy," Langmuir **18**, 5325–5328 (2002).

23. I. Kopf, J.-S. Samson, G. Wollny, C. Grunwald, E. Brüdermann, and M. Havenith, "Chemical imaging of microstructured self-assembled monolayers with nanometer resolution," J. Phys. Chem. C **111**, 8166–8171 (2007).

24. G. Wollny, E. Brüdermann, Z. Arsov, L. Quaroni, and M. Havenith, "Nanoscale depth resolution in scanning near-field infrared microscopy," Opt. Express **16**, 7453–7459 (2008).

25. J. Sun, J. C. Schotland, R. Hillenbrand, and P. S. Carney, "Nanoscale optical tomography using volume-scanning near-field microscopy," Appl. Phys. Lett. **95**, 121108 (2009).

26. A. A. Govyadinov, G. Y. Panasyuk, and J. C. Schotland, "Phaseless three-dimensional optical nanoimaging," Phys. Rev. Lett. **103**, 213901 (2009).

27. A. Cvitković, N. Ocelić, and R. Hillenbrand, "Analytical model for quantitative prediction of material contrasts in scattering-type near-field optical microscopy," Opt. Express **16**, 8550–8565 (2007).

28. N. Ocelić, "Quantitative near-field phonon-polariton spectroscopy," Dissertation, TU München (2007), Chapters 5 and 6.

29. M. Nonnenmacher, M. P. O'Boyle, and H. K. Wickramasinghe, "Kelvin probe force microscopy," Appl. Phys. Lett. **58**, 2921–2923 (1991).

30. M. Brehm, A. Schliesser, F. Čajko, I. Tsukerman, and F. Keilmann, "Antenna-mediated back-scattering efficiency in infrared near-field microscopy," Opt. Express **16**, 11203–11215 (2008).

31. B. Knoll and F. Keilmann, "Enhanced dielectric contrast in scattering-type scanning near-field optical microscopy," Opt. Commun. **182**, 321–328 (2000).

32. J. Renger, S. Grafström, L. M. Eng, and R. Hillenbrand, "Resonant light scattering by near-field-induced phonon polaritons," Phys. Rev. B **71**, 075410 (2005).

33. R. Esteban, R. Vogelgesang, and K. Kern, "Full simulations of the apertureless scanning near field optical microscopy signal: achievable resolution and contrast," Opt. Express **17**, 2518–2529 (2009).

34. K. Moon, E. Jung, M. Lim, Y. Do, and H. Han, "Quantitative analysis and measurements of near-field interactions in terahertz microscopes," Opt. Express **19**, 11539–11544 (2011).

35. J. D. Jackson, *Classical Electrodynamics*, 3rd ed. (Wiley, 1999), Section 4.4.

36. M. Brehm, "Infrarot-Mikroskopie mit einem Nahfeldmikroskop," Dissertation, TU München (2006), Chap. 4.

37. B. Wang and C. H. Woo, "Atomic force microscopy-induced electric field in ferroelectric thin films," J. Appl. Phys. **94**, 4053–4059 (2003).

38. E. D. Palik, *Handbook of Optical Constants of Solids* (Academic Press, New York, 1985).

39. T. Taubner, R. Hillenbrand, and F. Keilmann, "Nanoscale polymer recognition by spectral signature in scattering infrared near-field microscopy," Appl. Phys. Lett. **85**, 5064–5066 (2004).

40. L. Novotny, B. Hecht, and D. W. Pohl, "Implications of high resolution to near-field optical microscopy," Ultramicroscopy **71**, 341–344 (1998).

41. R. Krutokhvostov, A. A. Govyadinov, J. M. Stiegler, F. Huth, A. Chuvilin, P. S. Carney, and R. Hillenbrand, "Enhanced resolution in subsurface near-field optical microscopy," Opt. Express **20**, 593–600 (2012).

42. F. Demming, J. Jersch, K. Dickmann, and P. I. Geshev, "Calculation of the field enhancement on laser-illuminated scanning probe tips by the boundary element method," Appl. Phys. B **66**, 593–598 (1998).

43. N. Behr and M. Raschke, "Optical antenna properties of scanning probe tips: Plasmonic light scattering, tip–sample coupling, and near-field enhancement," J. Phys. Chem. C **112**, 3766–3773 (2008).

44. F. Huth, M. Schnell, J. Wittborn, N. Ocelić, and R. Hillenband, "Infrared-spectroscopic nanoimaging with a thermal source," Nature Mat. **10**, 352–356 (2011).
45. S. Amarie and F. Keilmann, "Broadband-infrared assessment of phonon resonance in scattering-type near-field microscopy," Phys. Rev. B **83**, 045404 (2011).
46. R. Hillenbrand, T. Taubner, and F. Keilmann, "Phonon-enhanced light-matter interaction at the nanometre scale," Nature (London) **418**, 159–162 (2002).
47. T. Taubner, F. Keilmann, and R. Hillenbrand, "Nanomechanical resonance tuning and phase effects in optical near-field interaction," Nano Lett. **4**, 1669–1672 (2004).
48. J. A. Porto, P. Johansson, S. P. Apell, and T. López-Ríos, "Resonance shift effects in apertureless scanning near-field optical microscopy," Phys. Rev. B **67**, 085409 (2003).

1. Introduction

Thin films, layered systems and buried structures are widespread in solid state physics and surface chemistry, as well as in optoelectronic and photonic devices. The investigation of layered samples with various microscopic techniques is therefore of substantial interest for their characterization and in order to detect small imperfections in the thickness or the material properties [1]. With the development of scattering-type scanning near-field optical microscopy (s-SNOM) [2, 3], the advantages of infrared light [4] as a non-destructive probe for matter have become available on a very local scale [5]. Infrared spectroscopic techniques are sensitive to the structural and chemical composition of a sample since the dielectric properties in this wavelength range are dominated by characteristic molecular or phononic absorption bands and features in the electronic band structure of solid states [4]. In s-SNOM the diffraction limit, which restricts the resolution of far-field optical methods to about half a wavelength [6], is circumvented by employing the evanescent fields at the apex of an illuminated sharp tip as a local probe with a wavelength-independent lateral resolution in the order of 10 nm [7].

Infrared s-SNOM has rapidly evolved into a versatile imaging technique for structural properties such as strain [8], crystalline polytypism [9], crystalline–amorphous phase boundaries [10], and for the mapping of free charge carriers [11]. It has been demonstrated that the near-fields are not only sensitive to the surface properties but also to the vertical composition under the investigated area [12, 13]. This effect can be used for substrate-enhanced near-field spectroscopy of thin polymer films [14], nanoparticles [15–17], and viruses [18], or for the characterization of superlenses [19], graphene [20], silicon dioxide films [21], and thin molecule layers down to monolayers [22–24]. Owing to these achievements, optical near-field microscopy has been suggested as a means for nanoscale optical tomography [25, 26].

However, the full three-dimensional reconstruction of the local dielectric function $\varepsilon(\mathbf{r})$ from the measured signals has not yet been demonstrated experimentally. As a step in this direction, we address translation invariant layered systems. Until now, approaches to describe s-SNOM experiments on layered samples require time-consuming simulations [21] or describe measured data qualitatively correctly, but are not sufficiently accurate for a quantitative analysis [14]. The finite dipole model (FDM) for homogeneous materials by Cvitković [27] and Ocelić [28] is an analytical and quantitatively very precise model for s-SNOM since the decay length of the near-fields at the tip is consistent with the experiment. We extend the FDM to multilayer samples and therefore provide a versatile and efficient framework for the prediction and analysis of s-SNOM signals.

Our experimental results for approach curves and probing depth on crystalline silicon samples covered with the polymer polymethylmethacrylat (PMMA) confirm the calculated curves. Moreover, the data demonstrates that the influence of the underlying material is still observable through 100 nm thick PMMA films, which is in agreement with earlier findings for silicon dioxide films [13, 21]. This huge influence of the substrate cannot be predicted with the point dipole model for layered systems, where already a 40 nm thick PMMA film shows a bulk-like

behavior [14]. Due to its accuracy, our model can be used as an analysis tool for the local characterization of thin films and the underlying material. Based on the calculation, we demonstrate that the near-field coupling in s-SNOM can be well characterized by an effective in-plane component of the wave vector, which is given by the shape of the tip. Using our model, we identify ways to optimize the experimental conditions in order to enhance the depth contrast in s-SNOM. Since we describe the tip–sample coupling electrostatically, the solution for the potential can also be applied to other scanning probe techniques such as Kelvin probe force microscopy [29].

The paper is organized as follows: In Sec. 2 we recapitulate the foundations of the FDM and present our extension to two-layered sample systems in an electrostatic approach. The agreement with our experimental data is demonstrated in Sec. 3, where also the results obtained from a point-dipole model including full retardation [14] are shown for comparison. In Sec. 4, we employ our model to determine how minor contrasts on the sample can be maximized in practice. Our findings are summarized in Sec. 5.

2. Modeling s-SNOM

In s-SNOM, dielectric samples are usually imaged using a metal-coated tip which, under illumination, acts as an optical antenna [5, 30]. The tip vibrates at a frequency Ω and the intensity of the back-scattered light is measured and demodulated at higher harmonic frequencies $n\Omega$ in order to suppress the contribution of the background scattered light [5]. Using a reference beam path, the signal can additionally be separated into amplitude S_n and phase ϕ_n [5].

The polarizability and scattering cross-section of the tip depends on its near-field coupling to the sample. Since the field amplitude of the backscattered light E_{sc} is proportional to the effective polarizability of the tip α_{eff}, a common approach of models describing s-SNOM experiments is to calculate α_{eff} as a function of the tip–sample distance H and the sample's dielectric properties. In the original point dipole model, the tip is represented by a discrete dipole with the polarizability of a sphere fitting the curvature of its apex [31]. α_{eff} is calculated by the electrostatic coupling to the fictive image dipole induced in the sample. A more sophisticated point dipole model was suggested by Aizpurua *et al.* [14], who included retardation by using an electrodynamic solution involving momentum-dependent reflection and transmission coefficients. This model can be applied to layered samples.

A drawback of the point dipole models is that their quantitative agreement with measured data is rather poor since the distance-dependency of the near-field coupling is not described realistically. A more accurate representation of the tip has to account for (i) a charge separation and (ii) the curvature at its apex. Most approaches to satisfy these requirements rely on numerical simulation techniques where an extended volume represents the tip [21, 30, 32, 33]. However, such simulations are usually time-consuming and inflexible to changes of geometric or dielectric values, especially if the oscillation of the tip is included.

In literature there are also analytical calculations in which the requirements above are taken into account. These models have the advantage to be computationally fast while being quantitatively precise. Moon *et al.* [34] introduced the self-consistent line dipole image method in which the exact electrostatic boundary conditions of a sphere interacting with a flat substrate are met. In the THz regime, they demonstrated an excellent agreement of their predictions with experimental data. An alternative approach in which the charge distributions within the tip and the sample are approximated by static point monopoles was developed by Cvitković and Ocelić in the scope of their finite dipole model (FDM) [27, 28]. In the mid-infrared spectral range, which is also addressed in this paper, they demonstrated that the FDM accurately describes s-SNOM measurements on homogeneous samples. However, in its original form, the FDM is not applicable to layered systems. The huge significance of thin films and protection layers

in recent nanostructures stimulated us to extend this model appropriately, in order to promote s-SNOM as a non-destructive characterization method for layered samples.

After an introduction to the FDM we propose an extension to the model that can handle layered samples. The implications of this extension are discussed at the end of this section.

2.1. Foundations of the FDM

In Fig. 1 the basic concept of the FDM [27,28] is illustrated. The tip is represented by a perfectly conducting spheroid which is polarized by a homogenous external field E_{in}. In the proximity of the high curvatures the resulting fields of the spheroid are approximated by opposite point charges $\pm Q_0$, which together form the dipole $p_0 \approx 2LQ_0$, where $2L$ is the length of the spheroid. Only the lower monopole Q_0 is assumed to be relevant for the near-field interaction with the sample. It induces a charge distribution close to the sample surface, the field of which in the upper half-space can be described by an image charge $-\beta Q_0$, where $\beta = (\varepsilon_2 - \varepsilon_1)/(\varepsilon_2 + \varepsilon_1)$ [35]. ε_1 and ε_2 are the dielectric functions of the surrounding medium and the sample, respectively (for air, $\varepsilon_1 = 1$).
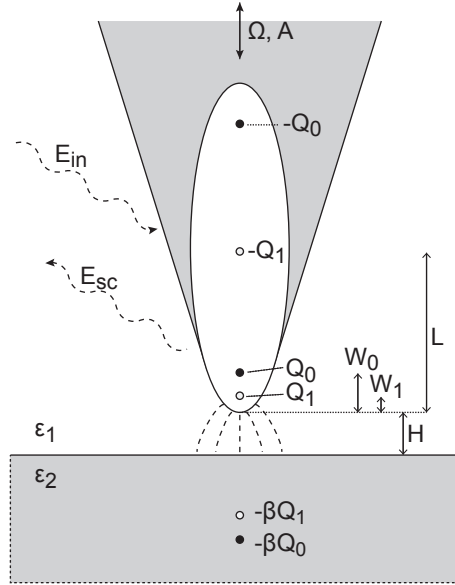

Fig. 1. Illustration of the FDM. A spheroid represents the tip. Its polarization in the external field E_{in} is approximated by the monopoles Q_0 and $-Q_0$ forming the dipole p_0. The near-field interaction with the sample is treated electrostatically by introducing virtual image charges $-\beta Q_0$ and $-\beta Q_1$ in the sample. In the tip, the near-field induced charges Q_1 and $-Q_1$ form the dipole p_1. E_{sc} is the propagating field scattered from the system. The bars on the right mark the position of the respective charges and the height H of the tip above the sample. ε_1 and ε_2 are the dielectric functions of the surrounding medium and the sample, respectively. The tip vibrates at a frequency Ω and an amplitude A.

The response of the spheroid to external monopole charges (i.e., to the image charges $-\beta Q_0$ and $-\beta Q_1$) is approximated by a near-field induced point monopole Q_1 at the position $W_1 \approx \rho/2$, different from the position $W_0 \approx 1.31\rho$ of Q_0 [27, 28]. (ρ is the radius of the tip.) With this assumption, which is an approximation of the actual image charge distribution within the spheroid, the curvature of the tip is considered. (For this approximation it is assumed that the tip is perfectly conducting.) A self-consistent treatment of the problem leads to the amount of

the induced charge Q_1 that has two contributions stemming from the polarization of the sample by Q_0 and by Q_1 itself [27, 28].

$$Q_1 = \beta(f_0 Q_0 + f_1 Q_1),\qquad(1)$$

where the functions f_0 and f_1 include the geometric properties of the system.

$$f_{0,1} = \left(g - \frac{\rho + 2H + W_{0,1}}{2L}\right)\frac{\ln\frac{4L}{\rho + 4H + 2W_{0,1}}}{\ln\frac{4L}{\rho}}.\qquad(2)$$

H is the vertical tip–sample separation and g is an empirical geometry factor, which describes the portion of the near-field induced charge in the tip, relevant for the interaction. For typical s-SNOM tip geometries, $|g| = 0.7 \pm 0.1$ [27, 28].

For the sake of charge neutrality an opposite point charge $-Q_1$ is introduced in the center of the spheroid. Together the induced charges form the dipole $p_1 \approx Q_1 L$, which is induced by the near-field interaction of the tip and the sample. The field of the back-scattered light E_{sc} is proportional to the effective polarizability α_{eff} of the tip, and can be calculated from the ratio between p_1 and p_0.

$$\alpha_{\mathrm{eff}} \propto \frac{p_1}{p_0} + 1 = \frac{1}{2}\frac{\beta f_0}{1 - \beta f_1} + 1.\qquad(3)$$

The tip vibration is accounted for by inserting

$$H(t) = H_0 + A(1 + \cos\Omega t)\qquad(4)$$

into α_{eff}, where H_0 is the minimum tip–sample separation, and A is the tip vibration amplitude. By calculating the respective Fourier component $\alpha_{\mathrm{eff},n}$ of $\alpha_{\mathrm{eff}}(t)$, the demodulation is regarded and the constant offset $+1$ in Eq. (3) can be neglected. The amplitude $S_n \propto |\alpha_{\mathrm{eff},n}|$ and phase $\phi_n \propto \arg(\alpha_{\mathrm{eff},n})$ correspond to the respective measured signals. Since the signal is usually evaluated in relation to a reference area on the sample, the proportionality given in Eq. (3) is sufficient for the calculation of a relative near-field contrast.

The measured scattering amplitude is additionally modified by a multiplicative factor $(1 + r)^2$, which takes into account the local far-field reflection coefficient r of the sample for the incident and the reflected propagating waves [14, 21, 36]. However, for the normalized signals in this paper, the modifications due to this factor are in the order of 10^{-3} and can therefore be neglected.

2.2. Extension to layered systems

We extend the FDM to bulk samples with one layer on top. In principle, the derivation in this section is also possible for more layers (cf. Appendix 6.1). The potential response Φ of the sample to the potential of a monopole Q in the distance z_0 above a flat layered sample can be calculated by solving the boundary conditions for the total potential U and its derivative perpendicular to the interfaces [37]. The height z of the cylindrical coordinate system (r, θ, z) is shown in Fig. 2(a). The potential above the sample is given by [37]

$$U = -\frac{Q}{4\pi\varepsilon_0}\left(\frac{1}{\sqrt{r^2 + z^2}} + \Phi\right).\qquad(5)$$

with

$$\Phi = \int_0^\infty A(k)\,e^{kz}J_0(kr)\,dk,\qquad(6a)$$

$$A(k) = e^{-2kz_0}\frac{\beta_{12} + \beta_{23}e^{-2kd}}{1 - \beta_{21}\beta_{23}e^{-2kd}},\qquad(6b)$$

where J_0 is the first kind Bessel function of zeroth order, ε_0 is the vacuum permittivity, ε_i are the involved dielectric functions as indicated in Fig. 2(a) ($i = 1, 2, 3$), and d is the thickness of the layer. The electrostatic reflection coefficient β_{ij} at an interface ij is defined by

$$\beta_{ij} = \frac{\varepsilon_i - \varepsilon_j}{\varepsilon_i + \varepsilon_j}. \tag{7}$$

In its sum representation for $|\beta_{12}\beta_{23}| < 1$, Eq. (6) can be converted into the result that Brehm [36] obtained by repeatedly mirroring the charge at the interfaces (cf. Appendix 6.2).
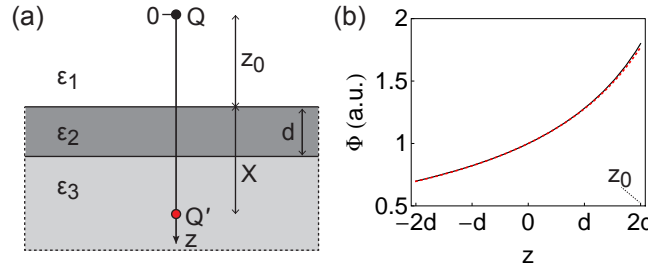

Fig. 2. (a) Monopole Q at the distance z_0 above the surface of a layered sample with one layer of thickness d. The definition of the z coordinate is needed in Eq. (6). ε_i are the dielectric functions. The potential response Φ of the sample is approximated by a monopole Q' at the distance X below the sample surface. (b) Comparison of the actual potential response Φ of a PMMA layer on silicon (black) with the approximation by a monopole Q' (red, dotted) for $z_0 = 2d$.

In order to employ the formalism of the FDM to layered systems, we approximate the potential response Φ by the potential of a point charge $Q' = -\beta_X Q$ at the distance X under the sample surface [cf. Fig. 2(a)]. For the determination of the strength and position of this point charge, we demand that its potential and electric field component in z-direction coincide with the actual response of the sample at $z = 0$:

$$\Phi|_{z=0} = \frac{-\beta_X}{z_0 + X}, \tag{8a}$$

$$\left.\frac{\partial \Phi(z)}{\partial z}\right|_{z=0} = \Phi'|_{z=0} = \frac{-\beta_X}{(z_0 + X)^2}. \tag{8b}$$

This condition leads to

$$\beta_X = -\left.\frac{\Phi^2}{\Phi'}\right|_{z=0}, \tag{9}$$

and

$$X = \left.\frac{\Phi}{\Phi'}\right|_{z=0} - z_0. \tag{10}$$

The inequality $X \neq z_0$ includes the asymmetry of the two half-spaces above and below the surface of the sample for layered samples.

In Fig. 2(b) the potential response Φ of a silicon sample covered by PMMA (dielectric data from Refs. [38, 39]) is compared to the potential of the monopole $Q' = -\beta_X Q$ for $z_0 = 2d$, i.e., the height of Q above the sample surface is twice the thickness of the layer. Around $z = 0$ the curves coincide as demanded. We found that for distances $z_0 > W_1$ and thicknesses d which are relevant to describe the tip–sample interaction, the point charge approximation matches well the actual potential response Φ in the region of the tip apex.

From the mathematical viewpoint, the evaluation of Q' is not restricted in the number, thickness, or dielectric properties of the sample materials. We confirmed the quality of the approximation for numerous material combinations and layer thicknesses. The largest deviation we found are in cases where the tip couples resonantly to a thin film on top of a dielectric substrate, as will be discussed in Sec. 3. We therefore recommend testing the quality of the approximation as demonstrated in Fig. 2(b), when employing our model to thin films with $\varepsilon_2 \approx -2$. In most cases, however, the approximation of Q' is very accurate and therefore the determination of Q_1 according to the formalism of the FDM is appropriate.

If $\beta_X^{(0,1)}$ and $X_{0,1}$ are evaluated for the respective height of Q_0 and Q_1, the FDM can be extended to layered samples by inserting a modified version of Eq. (2),

$$f_{0,1} = \left(g - \frac{\rho + H + X_{0,1}}{2L} \right) \frac{\ln \frac{4L}{\rho + 2H + 2X_{0,1}}}{\ln \frac{4L}{\rho}}, \tag{11}$$

and $\beta_X^{(0,1)}$ into Eq. (3). Our extended FDM can easily be implemented in mathematical software (like Wolfram Mathematica) and is computationally less intensive than numerical simulation techniques. The remaining FDM curves are based on the model introduced in this section.

2.3. Discussion

The FDM and our extension to layered samples comprise a very realistic quasi-analytical description of the electrostatic potential in the proximity of the tip apex. The model describes the mutual polarization of both tip and sample. It can therefore also be used to calculate potentials in scanning probe techniques that rely on electrostatic interactions if the two upper monopoles in Fig. 1 are omitted. Following Ref. [37], the calculation of the potentials within the sample is also possible with high accuracy.

Ocelić demonstrated that the electrostatic description of s-SNOM experiments in the framework of the FDM is valid in the mid-infrared spectral range [28]. From our extension we can draw further conclusions on the physical nature of the tip–sample coupling. The high lateral resolution of s-SNOM is due to the high in-plane components q of the wave vector $\mathbf{k}$, parallel to the surface of the sample [40]. Note that q is conserved at parallel interfaces of materials with different dielectric properties. In s-SNOM, a spatial frequency of ρ^{-1} can usually be resolved independently of the illuminating wavelength [7], thus there are in-plane components of $q^* \approx \rho^{-1}$ involved. For a tip radius ρ of 30 nm, q^* amounts to 3.3×10^5 cm^{-1}. This value is in good agreement with numerical simulations for the coupling of a sphere with the sample [20]. In Fig. 3(a) the Fresnel reflection coefficient r_p for transverse magnetic (TM) polarized light of silicon, PMMA and PMMA on silicon in different PMMA layer thicknesses is given as a function of q in the regime of evanescent waves ($q > k$, where k is the absolute value of the wave vector) according to Ref. [14]. Due to its elongated geometry, the tip is predominantly polarizable in the vertical direction. Thus, the TM polarized component of the light is dominant in the experiment. The aforementioned value for q^* is indicated in the plot.

For the bulk samples (red solid and dashed lines), $r_p(q)$ is nearly constant for large q. Hence, the electrostatic reflection coefficient $\beta = r_p(q \to \infty) \approx r_p(q^*)$ is a good approximation. In the case of layered samples, the black curves follow the silicon curve for low q, indicating a signal dominated by the underlying material, whereas for high q the signal is dominated by the PMMA film. Therefore, the simple approximation above ($q \to \infty$) is not valid for layered samples. Instead, we calculate the effective polarizability β_{eff} with our model as the weighted average of β_X^0 and β_X^1 [cf. Eq. (9)], where the weighting is done according to the ratio Q_1/Q_0. In Fig. 3(b), β_{eff} is evaluated depending on the height H of the tip above the respective samples for a tip radius ρ of 30 nm and a spheroid length L of 300 nm. For $H = 0$ we compare β_{eff} and
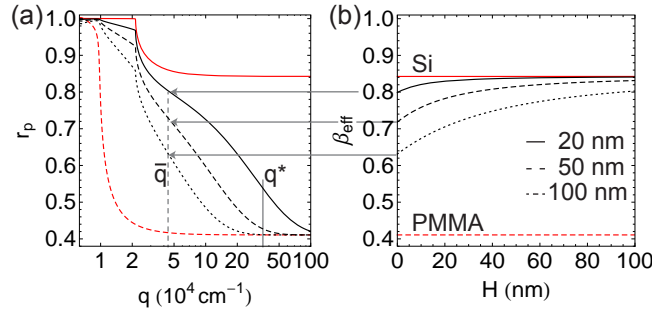
Fig. 3. (a) Fresnel reflection coefficient r_p depending on the in-plane component of the wave vector q in the regime of evanescent waves for TM polarized light, evaluated for a vacuum wavelength of 10 μm. The curves represent bare silicon (red, solid), bare PMMA (red, dashed), and PMMA-covered silicon with PMMA film thicknesses of 20, 50, and 100 nm. Horizontal arrows mark the respective values of β_{eff} for the tip being in contact with the sample. The values $q^* \approx \rho^{-1}$ and $\bar{q}$ are marked with the vertical gray lines. (b) Effective electrostatic reflection coefficients β_{eff} evaluated for a tip radius of 30 nm depending on the height H of the tip above the sample for the same samples as in (a).

$r_p(q)$ (gray arrows). The points of intersection in Fig. 3(a) are at $\bar{q} \approx 4.5 \times 10^4$ cm^{-1}, which is about one order of magnitude smaller than q^*. This discrepancy can be explained by the prolate geometry of the spheroid and demonstrates that the elongated geometry of s-SNOM tips is beneficial for a high imaging depth. With increasing height of the tip above the sample, β_{eff} increases. In Fig. 3(a) this translates into a lower effective in-plane component for the coupling for higher H. This is due to the faster decay of higher q in the evanescent range.

Since a single value for q cannot represent the actual angular spectrum of the fields, we interpret $\bar{q}$ as an effective in-plane component of the wave vector that describes the near-field coupling in s-SNOM. The high contributions in the range of $q^* \approx \rho^{-1}$ are most relevant for the lateral resolution at the surface of a sample. For the coupling, however, lower $q < q^*$ play a significant role that is noticeable especially when regions below the surface are addressed. Such low values are more dominant in the FDM, since the long axis L introduces an additional length scale that is not present in the point dipole model [21]. Herein lies an advantage in the representation of the tip as a spheroid instead of a sphere.

For other material combinations and other illumination wavelengths in the mid-infrared, we found roughly the same values for $\bar{q}$ as in Fig. 3 and conclude that $\bar{q}$ mainly depends on the values for ρ and L. This finding can be used for a very simple approximation of s-SNOM signals on layered systems with an arbitrary number of layers by employing the relation

$$\beta_{\text{eff}} \approx r_p(\bar{q}), \tag{12}$$

and following the procedure for homogeneous samples using Eq. (3). The exact value of $\bar{q}$ has to be determined from experimental data. However, the average height H_0 must stay constant and small for this simple approximation since only then is $X \approx H$ guaranteed.

3. Experimental validation

A fundamental difference between the finite dipole model and the point dipole model is the distance-dependent decay of the predicted near-fields in vertical direction z. The dipole field decays proportional to z^{-3} whereas the monopole field, which is dominant in the finite dipole model, decays proportional to z^{-2}. This difference is most prominent in so-called approach

curves where the back-scattered light intensity is measured as a function of the vertical tip–sample separation. In Fig. 4 we compare measured approach curves on silicon covered with 40 nm PMMA (red) with theoretical curves calculated according to the electrodynamic point dipole model [14] (black, dashed), and the FDM for layered systems (black, solid) for two different tip vibration amplitudes A in the second and third demodulation order. All curves are normalized to the scattering amplitude on a silicon surface for $H_0 = 0$.
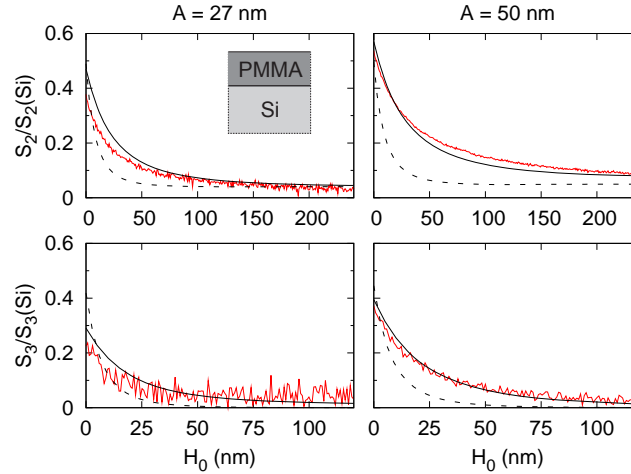

Fig. 4. Approach curves for the scattering amplitude on silicon covered with 40 nm PMMA at a tip vibration amplitude of $A = 27$ nm (left column) and $A = 50$ nm (right column) and two demodulation orders (upper row: $n = 2$, lower row: $n = 3$). The curves are normalized to the signal on bare silicon for $H_0 = 0$. Red line: experimental curve, black solid line: FDM calculation, black dashed line: point dipole approximation [14].

The measurements were performed in a commercial s-SNOM (Neaspec) with metallized tips (NanoWorld Arrow NCPt) at a wavelength of 10.59 μm (CO_2 Laser). Samples were prepared by spin-coating a PMMA/toluene solution onto silicon substrates and partly removing the polymer mechanically to uncover a reference area. The minimum distance where the full vibration amplitude A is reached ($H_0 = 0$) was carefully determined from the behavior of the mechanical signals. However, a deviation in the order of 2 nm cannot be excluded. For the calculations we used the values $\rho = 30$ nm, $L = 300$ nm, and $g = 0.7e^{0.06i}$ (according to Refs. [27, 28]). The dielectric functions are taken from Ref. [38] for silicon, and from the ellipsometry spectra by Röseler, which were used in Ref. [39]. We included in the calculations an experimentally determined constant background-contribution that we measured at a distance of 300 nm above the sample.

For all curves we find that the shape and the decay length is better represented by the FDM. The predicted decay according to the point dipole approximation is clearly too steep. Note that for $A = 27$ nm the determination of the exact position of $H_0 = 0$ in the experimental curves is not perfectly reliable on polymer samples. This could be the explanation for the slight offset close to $H_0 = 0$. The deviation for $A = 50$ nm at $n = 2$ can be attributed to the less efficient background suppression for high vibration amplitudes and low demodulation orders [28].

In order to demonstrate the possibility of directly extracting local dielectric properties from experimental data with our model, we used the approach curve for $A = 50$ nm at $n = 3$ to calculate back on the dielectric value ε_2 of the PMMA film. When assuming ε_2 to be purely real, we obtain the best match to the measurement for $\varepsilon_2 = 2.3 \pm 0.1$, which is very close to the literature value of $\varepsilon_2 = 2.39 + 0.08i$ [39].

To determine the influence of the substrate in different depths, we fabricated samples with PMMA film thicknesses between 40 nm and 115 nm. In Fig. 5 the measured scattering amplitudes, demodulated at $n = 3$ and $A = 50$ nm and normalized to bare silicon, are compared to the model prediction. The scattering amplitude is plotted against the height of the tip above the silicon substrate ($d + H_0$). The red dots mark the signal in contact with the respective sample ($H_0 = 0$). These values show a significant trend towards lower signals with increasing film thickness d. With increasing distance to the surface (H_0), the scattering amplitude decays towards the background level (red approach curves). We compare the measured data to our model. As in Fig. 4, the FDM prediction of approach curves (black, dashed) is in good agreement with the experimental curves. The solid black line coincides well with the scattering amplitude in contact (except for the value at $d = 54$ nm, for which the determination of $H_0 = 0$ was ambiguous) and shows an influence of the substrate over more than 100 nm. This finding confirms the numerically obtained results in Ref. [21] for SiO_2 films and agrees with earlier experiments [13]. The point dipole model [14] (black, dotted) predicts a saturation already at about $d = 40$ nm. This comparison demonstrates that s-SNOM is clearly more sensitive to the vertical composition of a sample than the widely-used point-dipole model predicts. The extended FDM can therefore help to quantify the influence of deeper sample regions.
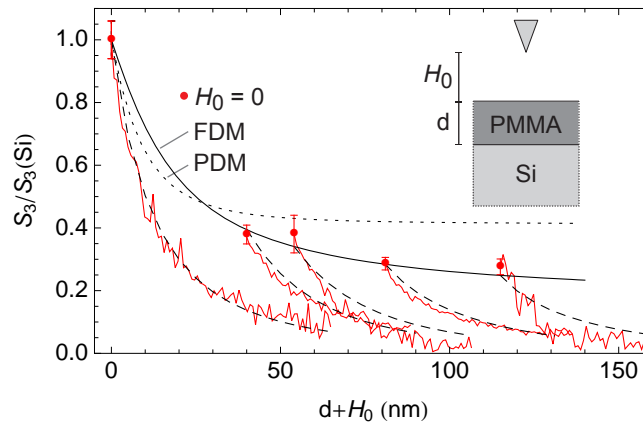

Fig. 5. Film thickness variation: Measured dependence of the scattering amplitude on a silicon sample covered by PMMA layers with thicknesses of $d = 0, 40, 54, 81, 115$ nm for $n = 3$ and $A = 50$ nm as approach curves (red curves). Red dots: Signals in contact ($H_0 = 0$). The bars mark the estimated error according to the uncertainty in the determination of H_0. Black solid line: FDM calculation of the scattering amplitude in contact; black dotted line: point dipole approximation (PDM) [14]; black dashed lines: FDM calculation of the approach curves ($H_0 > 0$).

Our calculation is also in good agreement with the measurements and numerically obtained results for the more complicated case of surface-phonon resonances in silicon dioxide thin films, published recently by Zhang *et al.* [21]. At the resonance position, however, we find slight quantitative deviations in the signal strength, which can be explained by the comparably low accuracy of the approximation of the potential response Φ by a point charge Q' in the special case of resonant coupling to a thin film (c.f. Sec. 2.2). Apart from that, our spectra are consistent with the shape of the experimental and theoretical curves in Fig. 2(a) and 2(b) of Ref. [21] and show the same thickness-dependent development of the spectral features.

In conclusion, our extension to the FDM is in good agreement with the experimental data and shows a correct distance-dependent coupling. This is essential for the quantitative analysis

of signals from deeper sample regions and enables us to make predictions helping to optimize experimental imaging parameters in order to maximize the sensitivity for the vertical structure of the sample.

4. Imaging parameters

Quantifying the influence of experimental imaging parameters, such as the tip vibration amplitude, the tip radius, and the illumination wavelength on the depth contrast helps to choose these quantities appropriately. In this section, we make theoretical predictions based on our extension to the FDM.

4.1. Influence of the tip

The influence of the PMMA layer thickness d on the signal S_2 is illustrated in Fig. 6(a) for different tip vibration amplitudes A. Since the reflectivity decreases with increasing layer thickness [cf. Fig. 3(a)], the curves are monotonously decreasing. With increasing amplitude A, the demodulated signal increases. However, this effect alone does not increase the relative contrast between different film thicknesses: The inset in Fig. 6(b) shows S_n depending on the layer thickness (or any other sample property). We assume the two points A and B to be close enough to treat the curve as linear. The relative contrast $S_{n,r}$ between the values S_n^A and S_n^B is then given by

$$S_{n,\mathrm{r}} := \frac{S_n^B}{S_n^A} = \frac{S_n^A + S_n'|_A \Delta}{S_n^A}, \tag{13}$$

where $S_n'|_A$ is the derivative at the point A. From Eq. (13) the *relative contrast change function*
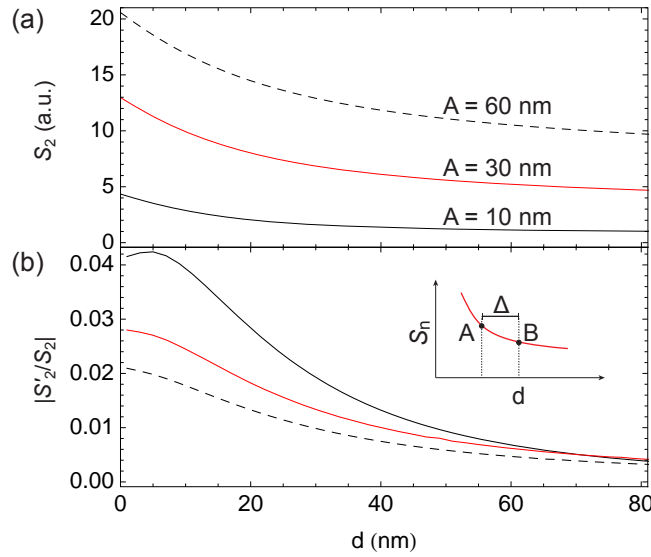

Fig. 6. (a) Demodulated scattering amplitude S_2 on a silicon sample covered by a PMMA layer of thickness d for the tip vibration amplitudes $A = 10$ nm (black), $A = 30$ nm (red), and $A = 60$ nm (black, dashed). (b) Relative contrast change function [Eq. (14)]. The inset is a sketch for the corresponding derivation in the main text.

$|S_n'/S_n|$ for small differences ($\Delta \to 0$) of a sample property can be derived to be

$$S_{n,\mathrm{r}} - 1 \propto \left| \frac{S_n'}{S_n} \right|. \tag{14}$$

This function is plotted in Fig. 6(b) for $n = 2$. It shows that higher contrasts can be expected for lower tip vibration amplitudes A and that the sensitivity to an inhomogeneity in thickness decreases with increasing thickness. A similar result based on the coupling of two point dipoles was derived recently by Krutokhvostov *et al.* for the resolution of buried metal particles [41].

An equivalent argumentation can be given for the desired tip radius ρ, as shown in Fig. 7. Here, the three curves represent three values for ρ at $A = 30$ nm. For sharp tips the field enhancement at the apex is higher than for tips with a high radius [42,43]. Therefore, also the light intensity scattered from the tip is higher for sharper tips [Fig. 7(a)]. For thin films ($d < 40$ nm), the relative contrast change function $|S_2'/S_2|$ is highest for sharp tips, meaning that they lead to a high contrast. For thicker films this advantage vanishes and blunt tips can even be beneficial in terms of contrast. Altogether we find that the tip radius is most relevant at the surface of the sample and slightly below. This could be due to the fast decay of near-field contributions with high in-plane components $q \approx \rho^{-1}$, as discussed in Sec. 2.
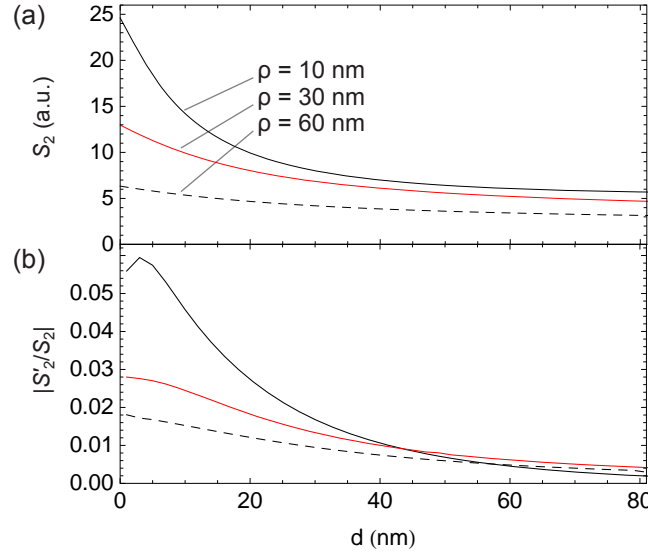

Fig. 7. (a) Demodulated signal S_2 on a silicon sample covered by a PMMA layer of the thickness d for the tip radii $\rho = 10$ nm (black), $\rho = 30$ nm (red), and $\rho = 60$ nm (black, dashed). The spheroid length is $L = 300$ nm in all cases. (b) Relative contrast change function [Eq. (14)].

In general, the maximization of the function $|S_2'/S_2|$ for a desired sample property can be a good theoretical starting point when searching for optimal imaging parameters. However, we emphasize that an optimization to high contrasts according to the definition in Eq. (13) is not always desirable, especially when tuning the tip vibration amplitude. Since the signals are low for low amplitudes, the noise disturbance will be high in this regime. It can therefore be useful to accept a lower relative contrast if the absolute difference in signals $|S_2^A - S_2^B|$ is higher. According to Fig. 6 this is fulfilled for higher amplitudes. In practice A has to be chosen in a way that the noise level is significantly below the demodulated scattering amplitude. With regard to the tip radius, Fig. 7 shows that for thin films sharp tips result in both high scattering amplitudes and high contrasts. Therefore sharp tips are also a good choice for investigating sample properties below the surface.

4.2. Spectral contrast

Recently, s-SNOM has made great advances as an instrument for local infrared spectroscopy [44, 45]. Therefore we investigated the influence of a thin protection layer on the spectral response of an underlying material. For such samples s-SNOM is a highly interesting imaging technique since it can extract information from below the surface in a non-destructive way. Figure 8 shows the demodulated scattering amplitude at $n = 2$ and $A = 30$ nm depending on the real part of the substrate dielectric function ε_3. We assume a constant imaginary part of $\text{Im}(\varepsilon_3) = 1$. In the plot, the scattering amplitudes of a sample with a 10 nm (black, solid), and 30 nm (red, solid) cover layer with $\varepsilon_2 = 2$ are compared to the respective signal in 0 nm (black, dotted), 10 nm (black, dashed), and 30 nm (red, dashed) height above the uncovered substrate.
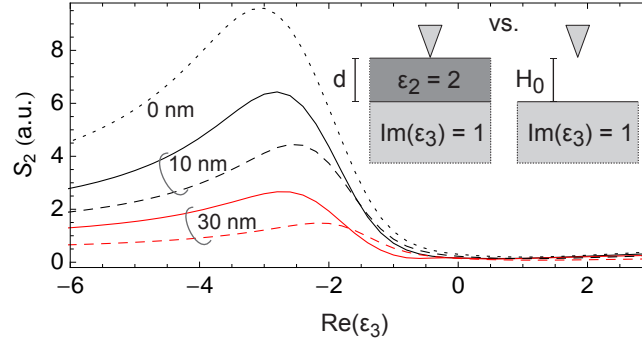

Fig. 8. Comparison of resonance curves. The demodulated scattering amplitude at $n = 2$ and $A = 30$ nm is shown depending on the real part of the substrate dielectric function. $\varepsilon_2 = 2$, $\text{Im}(\varepsilon_3) = 1$. Solid curves: $d = 10$ nm (black), $d = 30$ nm (red); dashed curves: $H_0 = 10$ nm (black), $H_0 = 30$ nm (red); dotted black curve: $d = 0$, $H_0 = 0$.

All curves show a resonant enhancement of the scattering amplitude between roughly $\text{Re}(\varepsilon_3) \approx -2.5$ and $\text{Re}(\varepsilon_3) \approx -2$. This is due to a pole in α_{eff} and can occur e.g. if surface polaritons are excited on the substrate [9, 32, 46]. High contrasts can therefore be expected between materials which show a high coupling to the tip and others which do not. The same argument holds if the dielectric function has a strong wavelength-dependency, as for example around phonon bands [9]. In this case a variation of the illuminating wavelength leads to a spectral contrast.

When comparing the resonance curves of the uncovered substrate (dotted and dashed), a shift of the resonance position with increasing tip–sample distance H_0 can be observed. This effect has also been observed experimentally on a silicon carbide substrate, where the illuminating wavelength was varied around a phonon resonance [47], and was predicted theoretically before [48]. If the substrate is covered by a thin, non-resonant film with $\varepsilon_2 = 2$ (solid curves), the coupling to the sample is higher as compared to the coupling through air. Additionally, the resonance shift with increasing layer thickness is smaller than the shift that occurs when increasing H_0 to the same extend on an uncovered substrate. This difference is relevant for the interpretation of spectrally resolved s-SNOM measurements on covered samples. Potentially, the resonance shift of a phonon resonance of a substrate material (like fused silica [45]) can also be used as a measure for the thickness of a thin film material on top. Similarly, the resonance position could give a hint on the depth of a buried object.

5. Conclusion and outlook

In this paper we have introduced an extension of the FDM to layered samples based on an electrostatic approach. We have shown that the model fits experimental data better than the point dipole model, which can be explained by the more realistic distance-dependent near-field decay under the spheroid of the FDM. For this reason, especially approach curves and signals from below the surface are represented better by the FDM. The fact that our model for layered systems is computationally fast makes it a good alternative to models which relay on time-consuming numerical simulations [21, 33]. Our model can quickly be applied to different samples and experimental situations and gives a good estimate of the expectable signals.

A quantitatively correct s-SNOM model can also be very helpful for the analysis of measured signals. For example, our model can be used to extract a local layer thickness by theoretically adjusting the parameter d, if the involved dielectric functions are known, as shown in Fig. 5. Also, it can help to get a deeper understanding of spectrally resolved measurements on thin films or of signals from samples which are protected by a capping layer (cf. Fig. 8). Both can be very helpful for the characterization of thin films or the underlying material. In future, we will also apply our model for the interpretation of s-SNOM measurements on superlenses.

For a practical use, we have demonstrated that measuring with sharp tips enhances the contrast that stems from regions below the surface. Low tip vibration amplitudes also increase the contrast but decrease the demodulated signal strength. Our work demonstrates that with s-SNOM the extraction of quantitative information on the vertical structure of a sample is possible through a polymer cover layer up to a thickness of about 100 nm.

From the solution to the Poisson equation, which leads to the potential response of a layered system [Eq. (6)], it can be seen that there is a fundamental difference between the distance-dependent tip–sample coupling on homogeneous samples and on layered samples. Whereas for homogeneous samples, β_{eff} is independent of the tip–sample distance (which is why the method of image charges can be applied [35]), the value varies with height for layered samples [cf. Fig. 3(b)] and resembles rather a series of image charges (cf. Appendix 6.2). This difference in the potential response of the sample is independent of the actual charge distribution, i.e., it holds independently of the assumed shape of the tip. When recording approach curves, the distance-dependent sample response is measured. We believe that a detailed analysis of the shape of low-noise approach curves (including the behavior of their slope) in different demodulation orders will reveal even more distinct information on the vertical structure of a sample.

Many polar materials have characteristic vibrational resonances in the infrared spectral range that result in high absorption while being transparent outside these resonances [4, 38]. In a multilayer system, it should therefore be possible to address a specific layer explicitly by tuning the illumination wavelength in a way that the respective layer is absorbing while the others are transparent. Spectrally resolved s-SNOM can therefore be used for the selective characterization of thin films in multilayer structures. The model presented in this paper allows analyzing and interpreting the measured spectra.

6. Appendix

6.1. Multilayer samples

In this paper, we introduced an extension to the FDM for samples with one thin film on top. Our formalism can easily be applied to multilayer samples, by deriving the coefficient $A(k)$ in Eq. (6) appropriately from the boundary conditions for the potential [37]. Here, we present the solution for a sample with three layers on top (surrounding medium: ε_1; layer 1: ε_2, d_1; layer 2:

ε_3, d_2; layer 3: ε_4, d_3; substrate: ε_5):

$$A(k) = \mathrm{e}^{-2kz_0} \frac{\beta_{12} + \beta_A \mathrm{e}^{-2k(d_1+d_2+d_3)}}{1 + \beta_B \mathrm{e}^{-2k(d_1+d_2+d_3)}},\tag{15}$$

with

$$\begin{aligned}\beta_A =\ & \beta_{12}\beta_{23}\beta_{34}\mathrm{e}^{2k(d_1+d_3)} + \beta_{12}\beta_{23}\beta_{45}\mathrm{e}^{2kd_1} + \beta_{12}\beta_{34}\beta_{45}\mathrm{e}^{2k(d_1+d_2)} + \\ & \beta_{23}\mathrm{e}^{2k(d_2+d_3)} + \beta_{23}\beta_{34}\beta_{45}\mathrm{e}^{2kd_2} + \beta_{34}\mathrm{e}^{2kd_3} + \beta_{45}\end{aligned}\tag{16}$$

and

$$\begin{aligned}\beta_B =\ & \beta_{12}\beta_{23}\mathrm{e}^{2k(d_2+d_3)} + \beta_{12}\beta_{23}\beta_{34}\beta_{45}\mathrm{e}^{2kd_2} + \beta_{12}\beta_{34}\mathrm{e}^{2kd_3} + \\ & \beta_{12}\beta_{45} + \beta_{23}\beta_{34}\mathrm{e}^{2k(d_1+d_3)} + \beta_{23}\beta_{45}\mathrm{e}^{2kd_1} + \beta_{34}\beta_{45}\mathrm{e}^{2k(d_1+d_2)}.\end{aligned}\tag{17}$$

6.2. Image charges

Brehm [36] derived an analytic extension to the electrostatic point dipole model for samples with one cover layer by repeatedly mirroring the dipole on both interfaces, using the method of image charges [35]. We verified that the general potential response given in Eq. (6) is identical with the potential response that can be calculated from a series of image charges in the sample for the case that the series converges ($|\beta_{12}\beta_{23}| < 1$). The mathematical identities

$$\frac{1}{1 - \beta_{12}\beta_{23}\mathrm{e}^{-2kd}} = \sum_{m=0}^{\infty} (\beta_{21}\beta_{23})^m \mathrm{e}^{-2mkd},\tag{18}$$

for $|\beta_{12}\beta_{23}| < 1$, and

$$\int_0^{\infty} \mathrm{e}^{-k|z|} J_0(kr)\,dk = \frac{1}{\sqrt{z^2 + r^2}}\tag{19}$$

enable a transformation of Eq. (6) into

$$\Phi = \beta_{12}\frac{1}{2z_0 - z} + \gamma_{12}\gamma_{21}\sum_{m=1}^{\infty}\frac{\beta_{21}^{m-1}\beta_{23}^m}{2z_0 - z + 2md}\tag{20}$$

for $r = 0$. The electrostatic transmission coefficient γ_{ij} is given by $\gamma_{ij} = \beta_{ij} + 1$ and $\beta_{ij} = -\beta_{ji}$. This result is identical with the potential of a series of image charges

$$\begin{aligned}R_0 &= \beta_{12}Q, & \text{(21a)}\\ R_{m>0} &= \gamma_{21}\beta_{21}^{m-1}\beta_{23}^m\gamma_{12}Q & \text{(21b)}\end{aligned}$$

at the position $z_m = z_0 + 2md$ under the sample surface which was derived by Brehm [36].

The constraint $|\beta_{12}\beta_{23}| < 1$ or $|(\varepsilon_1 - \varepsilon_2)(\varepsilon_2 - \varepsilon_3)| < |(\varepsilon_1 + \varepsilon_2)(\varepsilon_2 + \varepsilon_3)|$ for which the series converges limits the practicality of this representation dramatically. Many material resonances of practical relevance, such as the optically excited phonon resonances in silicon carbide or silicon dioxide cannot be calculated in the series approach. This restriction can be avoided by using the integral representation given in Eq. (6).